Structure of Alkanoic Acid Stabilized Magnetic Fluids. A Small-Angle Neutron and Light Scattering Analysis

Lifen Shen, Agnieszka Stachowiak, Seif-Eddeen K. Fateen, Paul E. Laibinis,* and T. Alan Hatton*

Department of Chemical Engineering, Massachusetts Institute of Technology, Cambridge, Massachusetts 02139

Received December 23, 1999. In Final Form: September 25, 2000

Small-angle neutron scattering and dynamic and static light scattering measurements were used to probe the structures of aqueous and organic-solvent-based magnetic fluids comprising dispersed magnetite nanoparticles (∼10 nm in diameter) stabilized against flocculation by adsorbed alkanoic acid layers. A core−shell model fitted to a set of neutron scattering spectra obtained from contrast variation experiments allowed the determination of the iron oxide core size and size distribution, the thicknesses of the surfactant shells, and the spatial arrangement of the individual particles. The magnetic colloidal particles appear to form compact fractal clusters with a fractal dimension of 2.52 and a correlation length of ∼350 Å in aqueous magnetic fluids, consistent with the structures of clusters observed directly using cryo-TEM (transmission electron microscopy), whereas chainlike clusters with a fractal dimension of 1.22 and a correlation length of ∼400 Å were found for organic-solvent-based magnetic fluids. The differences in cluster structure were attributed to the relative strengths of the particle−particle interaction energies. Weak interactions in the organic-solvent-based systems dictate the formation of small structures for which the apparent fractal dimensions are naturally small, whereas significantly stronger interparticle interactions in aqueous magnetic fluids result in larger, more compact clusters with higher fractal dimensions. The growth of the aqueous clusters beyond a certain size was inhibited by an increasingly high energy barrier (balance between repulsive electrostatic and attractive van der Waals interactions) with increasing cluster size. The aqueous clusters were stable against further growth when diluted with a surfactant solution but grew in time when diluted with pure water. In the latter case, the loss of part of the stabilizing secondary surfactant layer to the aqueous phase to satisfy thermodynamic partitioning constraints led to a destabilization in its dispersion. Light scattering studies indicated a change in the fractal dimension from 2.52 to about 1.20 as the clusters grew.

1. Introduction

Magnetic fluids can be prepared as colloidal suspensions of single-domain magnetic nanoparticles (∼10 nm in diameter) stabilized against flocculation and settling by surfactants or polymers adsorbed on their surfaces.[1] Owing to their unique physical and chemical properties, these ferromagnetic liquids have attracted much interest since their inception in the mid-1960s, and since then there have been many suggested and realized commercial applications of ferrofluids.[2−4] The performance and stability of the fluids are controlled by the nature of the particle−particle interactions which in turn are dictated by the surfactant or polymer layers coating the particles.[5] It is the goal of this work to elucidate the particle and solution structure of a certain class of fatty acid stabilized magnetite nanoparticle suspensions.

We have synthesized a range of organic and water-based magnetic fluids using chemical precipitation methods.[6] The precipitated magnetite nanoparticles were first coated with a primary layer of fatty acids chemisorbed to the iron oxide surfaces; these particles were easily dispersed in nonpolar hydrocarbon solvents, such as hexane, which readily solvated the surfactant hydrocarbon chains extending from the particle surface. To prepare aqueous magnetic fluids, a secondary surfactant (also a fatty acid) was coated on the particles to form a bilayer with the primary surfactants such that the exposed secondary surfactant headgroups provided a charged, hydrophilic interface for the formation of stable, water-based dispersions. This two-step synthetic approach also allows for the introduction of other secondary surfactants and the tuning of the surface properties of these magnetic fluids for a range of targeted applications. In previous work, we have inferred from thermogravimetric analysis (TGA) results that two distinct populations exist within the surfactant coating, corresponding to the two fatty acid layers coating the particles. A phase transition detected by differential scanning calorimetry (DSC) suggested a partial interpenetration of the hydrocarbon tails of the primary and secondary surfactants. The core magnetite particle size distribution was determined to follow a log-normal distribution using transmission electron microscopy (TEM). These analyses were all performed on dried samples, and the results may be subject to sample preparation artifacts such that they do not reflect the actual characteristics of the coated nanoparticles in suspension. In the present work, therefore, we have used small-angle neutron scattering (SANS) and dynamic and static light scattering to provide in situ measurements and direct characterization of the microstructure of surfactant-stabilized nanoparticle dispersions in both aqueous and organic solvents.

SANS is a powerful tool for elucidating the structure of colloidal systems such as micelles, microemulsions, and

(1) Rosensweig, R. E. *Ferrohydrodynamics*; Cambridge University Press: Cambridge, 1985.
(2) Berkowitz, A. E.; Lahut, J. A.; Vanburen, C. E. *IEEE Trans. Magn.* **1980**, *MAG-16*, 184.
(3) Berkovsky, B. M.; Medvedev, V. F.; Karkov, M. S. *Magnetic Fluids: Engineering Application*; Oxford University Press: New York, 1993.
(4) Raj, K.; Moskowitz, R. *J. Magn. Magn. Mater.* **1990**, *85*, 233.
(5) Pieters, B. R.; Williams, R. A.; Webb, C. *Magnetic Carrier Technology*; Butterworth-Heinemann Ltd: Oxford, 1992.
(6) Shen, L. F.; Laibinis, P. E.; Hatton, T. A. *Langmuir* **1999**, *15*, 447.

10.1021/la9916732 CCC: $20.00
Published on Web 12/14/2000

nanoparticle dispersions.[7,8] As protons and deuterons have distinctly different neutron scattering abilities, the scattering patterns of microstructured fluids can be easily altered by substitution of deuterated analogues for specific chemical components in the system to emphasize and probe selected microdomains within these colloidal dispersions. In addition to providing information on the structural characteristics of the individual particles, SANS also provides information on interparticle interactions and cluster formation within colloidal systems, even at reasonably high concentrations.[9] In this paper, for instance, we present scattering measurements for a series of fatty acid stabilized magnetic fluids with variously deuterated regions within the dispersions. This deuteration accentuated different domains relative to others to provide the needed discrimination for estimation of domain properties such as particle core size, bilayer thickness, and solvent penetration of the surfactant layers. The SANS spectra were analyzed by performing model-dependent fits to extract information both on the internal structure of the individual particles[10−13] and on the correlation between these nanoparticles. The results confirm a layered microstructure of highly organized surfactants on the magnetic particles and suggest that the particles form small clusters in suspension, the nature of which depends on whether the systems are aqueous or organic-based. When combined with light scattering measurements and suitable estimates of magnetic, van der Waals, and electrostatic interaction energies, these SANS results provide additional insight into the geometric arrangement of the nanoparticles in the fluids, that is, whether they form compact spherical clusters or chainlike aggregates.

2. Experimental Section

Materials. Deuterated decanoic acid ($CD_3(CD_2)_8CO_2H$, density = 0.893 g/cm^3, 98%), deuterated dodecanoic acid ($CD_3(CD_2)_{10}CO_2H$, density = 0.883 g/cm^3, >98%), and deuterium oxide (D_2O, density = 1.1044 g/cm^3) were obtained from Cambridge Isotope Laboratories (Andover, MA). Iron(II) chloride tetrahydrate (99%), iron(III) chloride hexahydrate (97%), ammonium hydroxide (28% NH_3 in water, double distilled), decanoic acid (99%), and dodecanoic acid (99.5%) were obtained from Aldrich (Milwaukee, WI). Acetone and methanol were obtained from Mallinckrodt (Paris, KY). All chemicals were used as received.

Preparation of Magnetic Fluids. Magnetite (Fe_3O_4) nanoparticles were produced by the chemical coprecipitation of Fe(II) and Fe(III) chloride from an aqueous solution by the addition of ammonium hydroxide (NH_4OH). These iron oxide clusters were coated with a primary surfactant during the precipitation process. The excess primary surfactant was removed by washing the suspension with acetone. Oil-based magnetic fluids were made by redispersing the primary-surfactant-coated iron oxide nanoparticles in the desired solvent (e.g., hexane in the present study), with the aid of ultrasonication when necessary. To make aqueous magnetic fluids, the primary-surfactant-stabilized particles were coated with a secondary surfactant to form a self-organized bilayer of the two surfactants on the surface of the iron oxide nanoparticles, as illustrated schematically in Figure 1. Detailed information on the synthesis is reported elsewhere.[6] In the present study, we used decanoic acid (C_{10}) and lauric acid (C_{12}) as primary and secondary surfactants, respectively. We prepared samples using protonated and/or deuterated fatty acids for the primary and secondary surfactants and water as the solvent. The scattering length densities (SLD) of the components are summarized in Table 1. For the contrast variation studies, we also prepared magnetic fluids with water of different D_2O/H_2O compositions.

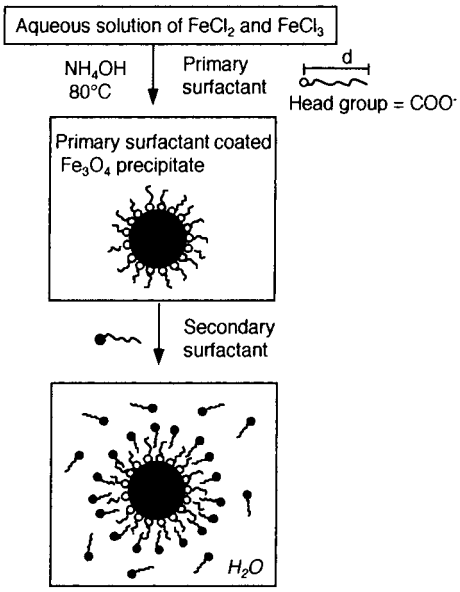

Figure 1. Synthesis of surfactant bilayer stabilized magnetic fluids using fatty acids as the primary and secondary surfactants to produce stable aqueous magnetic fluids.

Table 1. Experimental Design: Scattering Length Densities (10^{-6} Å^{-2}) for Different Components in the Magnetic Nanoparticles

	aqueous fluid Figure 2 (protonated surfactants)	aqueous fluid Figure 3 (deuterated primary layer)	organic fluid Figure 4 (protonated surfactant)
iron oxide	6.96	6.96	6.96
primary surf (C_{10})	0.22	5.76[a]	0.22
secondary surf (C_{12})	0.18	0.18	
solvent	−0.56 to 6.36[a]	−0.56 to 6.36[a]	−0.48 to 6.68[a]

[a] Deuterated chemicals.

SANS Measurements. Neutron scattering experiments were performed on the NG3 30 m spectrometer at the National Institute of Standards and Technology (NIST) in Gaithersburg, MD. Unpolarized neutrons of wavelength $\lambda = 6$ Å with a spread of $\Delta\lambda/\lambda = 15\%$ were focused on samples held in 1 mm quartz cells. An overall q range of 0.0046−0.3294 Å^{-1} was achieved by using three sample-to-detector distances of 13, 6.5, and 2 m with a 25 cm detector offset, where $q = (4\pi/\lambda)\sin(\theta/2)$ is the magnitude of the scattering vector and θ is the scattering angle. Scattering from the samples was corrected for background and empty cell scattering. The sensitivity of individual detector pixels was normalized by comparison to the isotropic scattering of water. In our model fitting, we found that because of the strong scattering signals from our fluid samples, the correction for free secondary surfactant was insignificant. The scattering data sets were circularly averaged and placed on an absolute scale by using flux ratios measured through a series of pinholes and standards and software supplied by NIST. Instrumental smearing was assumed to be negligible for the instrumental configuration and wavelength spread used in this work.[14]

TEM and SQUID Studies of the Particle Size Distribution. The particle size and its distribution for the iron oxide core of the magnetic particles were studied using bright field TEM (Akashi 002B, 200 kV). The magnetization of the diluted samples was measured using a superconducting quantum interference

(7) Windsor, C. G. *J. Appl. Crystallogr.* **1988**, *21*, 582.
(8) Chen, S. H. *Annu. Rev. Phys. Chem.* **1986**, *37*, 351.
(9) Hayter, J. B. *J. Appl. Crystallogr.* **1988**, *21*, 737.
(10) Cebula, D. J.; Charles, S. W.; Popplewell, J. *Colloid Polym. Sci.* **1981**, *259*, 395.
(11) Hayter, J. B. *J. Chem. Soc., Faraday Trans.* **1991**, *87*, 403.
(12) Boue, F.; Cabuil, V.; Bacri, J. C.; Perzynski, R. *J. Magn. Magn. Mater.* **1993**, *122*, 78.
(13) Pynn, R.; Hayter, J. B.; Charles, S. W. *Phys. Rev. Lett.* **1983**, *51*, 710.
(14) Pedersen, J. S.; Posselt, D.; Mortensen, K. *J. Appl. Crystallogr.* **1990**, *23*, 321.

device (SQUID) magnetometer (Quantum Design, MPMS) at room temperature. Detailed procedures for these experiments were as described elsewhere.

Cryogenic TEM Measurements. A few (2−3) microliters of an aqueous magnetic fluid suspension stored at 25 °C in a controlled environment vitrification system (CEVS, University of Minnesota; the temperature within the CEVS box is controlled precisely, and the relative humidity is kept at >90%) were withdrawn in a pipet, deposited on a specially prepared lacey carbon electron microscope grid, and blotted to remove excess liquid. This processing took place within the CEVS unit, preventing water evaporation and temperature changes in the sample. The grid bearing the sample was plunged into a liquid ethane reservoir cooled by liquid nitrogen to a temperature close to its freezing point. The rapid heat transfer away from the grid vitrified the sample. The specimen was transferred under liquid nitrogen to the cooled tip of a cryotransfer stage (CT3500J, Oxford Instruments) which was then inserted under positive dry nitrogen pressure into the JEOL 1200 TEM and imaged at slight underfocus (1−3 μm). The sample temperature was maintained at −165 °C at all times during imaging, to prevent the amorphous-to-crystalline phase transformation in ice.

Light Scattering Measurements. Hydrodynamic radii of the magnetic nanoparticles were determined using a Brookhaven model BI-200SM laser light scattering system (Brookhaven Instrument Corp.) at a wavelength of 514 nm and a scattering angle of 90°. Static light scattering experiments were performed over the scattering angle range of 20−150°.

3. Analysis

3.1. Small-Angle Neutron Scattering. Neutron scattering from magnetic nanoparticle suspensions is caused both by direct interactions of neutrons with the nuclei of atoms within the particles and by interactions between the magnetic dipoles of the neutrons and those of the unpaired electrons in the iron oxide magnetic particles. For a monodisperse colloidal system, the nuclear scattering component of the intensity spectrum is given by

$$I_N(q) = N_p|F_N(q)|^2\ S(q) \qquad (1)$$

where $q = (4\pi/\lambda)\sin(\theta/2)$ is the scattering vector, N_p is the particle number density, and $S(q)$ is the interparticle structure factor, reflecting the center-to-center pair correlation function for the particles. The particle form factor, $F_N(q)$, accounts for the scattering from all atoms in the particle, weighted by the phase shifts corresponding to their relative atomic positions r within the particle, that is, by $\exp(iq\cdot r)$, and is given by the integral

$$F_N(q) = \int_{\text{particle } i}(\rho_i(r) - \rho_s)\exp(iq\cdot r)\ \mathrm{d}^3r \qquad (2)$$

The neutron scattering length density (SLD) of a substance, ρ, can be computed using the known neutron scattering lengths of individual atoms and the stoichiometric chemical formula of the compound. The subscripts i and s designate particle i and the solvent, respectively.[8] The positional dependence of ρ_i reflects the spatial heterogeneity within the particle i; in our case, the iron oxide cores and surfactant shells can have very different SLDs.

The contribution to the overall neutron scattering intensity patterns resulting from the magnetic dipole−dipole interactions is, for unpolarized neutrons,

$$I_M(q) = [1 - (\mathbf{H}\cdot\mathbf{q})^2]N_p|F_M(q)|^2S(q) \qquad (3)$$

where

$$F_M(q) = \int_{\text{particle } i}\rho_M\exp(iq\cdot r)\ \mathrm{d}^3r \qquad (4)$$

and **H** and **q** are unit vectors in the direction of the magnetization and scattering, respectively.[11,15] In the absence of an external magnetic field, the magnetic particles orient randomly in all directions and the scattering is isotropic. Under these conditions, the orientational term can be averaged over all magnetization directions and reduces to $[1 - (\mathbf{H}\cdot\mathbf{q})^2] = {}^2/_3$. The magnetic scattering length density, ρ_M, for a molecule can be calculated knowing the magnetic scattering amplitudes, p, of the individual species within the molecule. For a point dipole of S Bohr magnetons, we have $p = 0.27S \times 10^{-12}$ cm, which indicates that magnetic scattering amplitudes depend on the valence of the atom or ion, in contrast to nuclear scattering amplitudes, which depend only on the identity of the atom or ion nucleus. For example, Fe, Fe^{2+}, and Fe^{3+} ($S = 2$, 4, and 5, respectively) have different magnetic scattering length densities (0.6×10^{-12}, 1.08×10^{-12}, and 1.35×10^{-12} cm, respectively) but have the same neutron scattering length density of 0.96×10^{-12} cm.[16] Because magnetic scattering by oxygen can be neglected,[17] the magnetic SLD for Fe_3O_4 can be estimated to be 5.06×10^{-6} Å^{-2}, which is approximately 70% of the nuclear SLD. This estimate indicates that for a spherical iron oxide particle of radius 50 Å, the magnetic scattering contributes about 20% to the neutron scattering in the higher q range and cannot be ignored in the analysis of experimental SANS spectra.

Because there is no coherence between the nuclear and magnetic scattering, the two intensity components are additive. In our case, the scattering intensity in nonmagnetized, monodisperse ferromagnetic samples can be described by

$$I(q) = I_N(q) + I_M(q) = N_p\left(\left|F_N(q)\right|^2 + \frac{2}{3}\left|F_M(q)\right|^2\right)S(q) \qquad (5)$$

For a polydisperse system, the neutron scattering intensity distribution is

$$I(q) = N_p\left[\int_0^\infty\left(\left|F_N(q)\right|^2 + \frac{2}{3}\left|F_M(q)\right|^2\right)P(x)\ \mathrm{d}x\right]S(q) \qquad (6)$$

where $P(x)$ is the particle size probability density distribution. TEM measurements indicate that the particles have a log-normal size distribution, that is,

$$P(x) = \frac{1}{\sqrt{2\pi}\sigma x}\exp[-(\ln(x) - \mu)^2/2\sigma^2] \quad (x > 0) \qquad (7)$$

where $x = D/D_p$ is the reduced diameter, with D_p being the median of the particle diameter D.[18] The mean and the standard deviation of $\ln(x)$ are given by μ and σ, respectively, and the mean of x itself is given by $\exp(\mu + \sigma^2/2)$, with variance $[\exp(\sigma^2) - 1]\exp(2\mu + \sigma^2)$.

The above set of equations provides a general description of scattering by a polydisperse suspension of magnetic nanoparticles. In the next two sections, we describe the specific models used for the two form factors and the interparticle structure factor in the analysis of our SANS spectra.

3.1.1. Form Factor. The form factor can be calculated from an appropriate structural model of the scattering particles. For a uniform sphere of scattering length density ρ, volume V_p, and radius R, the form factor $F(q)$ can be

(15) Lin, D.; Nunes, A. C.; Majkrzak, C. F.; Berkowitz, A. E. *J. Magn. Magn. Mater.* **1995**, *145*, 343.
(16) Sears, V. F. *Neutron News* **1992**, *3*, 26.
(17) Hayter, J. Private communication.
(18) Buhrman, R. A.; Granqvist, C. G. *J. Appl. Phys.* **1976**, *47*.

written as

$$F(q) = V_p(\rho - \rho_s)\frac{3j_1(qR)}{qR} \quad (8)$$

where $j_1(x) = (\sin x - x \cos x)/x^2$ is the first-order spherical Bessel function.[8] This is the appropriate function for $F_N(q)$ when nuclear scattering is by the iron oxide cores only, that is, when there is no contrast between the solvent and the stabilizing surfactant layers. Because the iron oxide core provides the only contribution to magnetic scattering under all solution conditions, this form factor was also used for all magnetic scattering calculations, with the one caveat that it was necessary to account for a nonmagnetic layer on the iron oxide surface in selecting an appropriate magnetic radius for the calculations. For magnetite, Rosensweig has suggested that this layer is approximately 8.3 Å thick, corresponding to the lattice constant of the cubic structure of the iron oxide crystals,[1] a value close to the difference in mean particle sizes found using TEM and magnetization measurements. Thus, in our analyses we assumed the magnetic radius to be 8.3 Å smaller than the nuclear scattering radius; that is, $R_M = R_N - 8.3$ Å.

The form factor for a spherical particle with an internal core of radius R_1 and SLD ρ_1 surrounded by a shell with an outer radius R_2 and SLD ρ_2 is given by

$$F(q) = \frac{4}{3}\pi {R_1}^3(\rho_1 - \rho_2)\frac{3j_1(qR_1)}{qR_1} + \frac{4}{3}\pi {R_2}^3(\rho_2 - \rho_s)\frac{3j_1(qR_2)}{qR_2} \quad (9)$$

Extension of the form factor to particles having a spherical core with two or more shells is straightforward.

3.1.2. Structure Factor. A number of theoretical and experimental studies on colloidal systems consisting of silica, gold, and smoke particles suggest that colloidal aggregation processes lead to scale-invariant fractal structures.[19−22] We have therefore assumed that the particles in our magnetic fluids aggregate as small fractal clusters and have used an appropriate fractal model formulation for $S(q)$ to capture salient features of these aggregates. In adopting such a structural model, we acknowledge the difficulty of treating rigorously the various coupled interactions existing in a magnetic fluid and have used a phenomenological description of the outcome of these complicated interactions between the particles. It must be noted that the hard sphere steric interaction model commonly used to describe interparticle correlations in colloidal suspensions could not provide a satisfactory description of our results. $S(q)$ for a hard sphere potential was close to unity over the entire q range studied,[23] even for the most concentrated samples used in our experiments, in direct contrast to the sharp changes in the low-q region of the spectrum observed experimentally. A fractal structure is defined by the relationship that the average mass M of a medium inside a sphere with a diameter equal to the fractal correlation length ξ varies as ξ^D, where D is the fractal dimension,[24] which must be less than or equal to the Euclidean dimension of 3. A value of D close to 3 is obtained for a dense medium, whereas a fractal dimension near unity indicates a loosely connected network. The structure factor $S(q)$ for fractal clusters of particles of uniform radius $R = R_C + t$ (R_C is the particle radius and t is the (bi)layer thickness) is given by[25]

$$S(q) = 1 + \frac{1}{(qR)^D}\frac{2D\Gamma(D-1)}{[1 + (q\xi)^{-2}](D-1)} \times \sin[(D-1)\tan^{-1}(q\xi)] \quad (10)$$

It is assumed here that the clusters themselves do not interact, as reflected in the derivation of eq 4, where a cutoff factor $\exp(-r/\xi)$ was introduced into the pair correlation function to limit long-range interactions between clusters.[26] Aggregates were also assumed to be of uniform correlation length, which implicitly required that all particles participated in these clusters and that there were no free particles in solution. The validity of this assumption was checked by comparing the structure factor calculated assuming a Gaussian distribution of cluster correlation lengths to the $S(q)$ for monodisperse fractal aggregates. Our DLS studies indicated that the polydispersity of these aggregates did not exceed 30%, for which our estimated error at the lowest q values used experimentally was less than 7%. Over the range of higher q values where $F(q)$, which captures the intraparticle features, is important, the error introduced by assuming monodisperse aggregates is negligible.

Several workers have reported that the fractal interparticle structure factor is unaffected by the primary particle size distribution.[27] The particle polydispersity was, therefore, not incorporated into the fractal model, and the mean particle size (iron oxide particle core and its stabilizing surfactant layer(s)) was used in the model. Our sensitivity study showed that $S(q)$ is more sensitive to the changes in R and D than to those in ξ. This is probably a direct consequence of the choice of the exponential cutoff function implicit in the structure factor used here, which makes the structure factor fairly broad in the transition region, thereby masking small cluster polydispersity effects.[28−30]

3.2. Static Light Scattering. The length scale probed by any scattering technique is determined by the accessible q range of the instrument, roughly as indicated by the relationship, $q \sim 2\pi/R$. Because the scattering vector is inversely proportional to wavelength λ and the neutron and laser beams used in our study have wavelengths of 0.6 and 514 nm, respectively, light scattering allows the study of the internal structure of larger aggregates at a much smaller q range than is possible with neutron scattering.

For large aggregates for which the correlation length, ξ, exceeds the length scale q^{-1} probed by the scattering,

(19) Schaefer, D. W.; Martin, J. E.; Wiltzius, P.; Cannell, D. S. *Phys. Rev. Lett.* **1984**, *52*, 2371.
(20) Weitz, D. A.; Huang, J. S. In *International Topical Conference on Kinetics of Aggregation and Gelation*; Elsevier Science Publishers B.V.: Athens, GA, 1984; p 19.
(21) Zhang, Y.; Meriani, S. *J. Appl. Crystallogr.* **1994**, *27*, 782.
(22) Dimon, P.; Sinha, S. K.; Weitz, D. A.; Safinya, C. R.; Smith, G. S.; Varady, W. A.; Lindsay, H. M. *Phys. Rev. Lett.* **1986**, *57*, 595.
(23) Mortensen, K.; Pedersen, J. S. *Macromolecules* **1993**, *26*, 805.
(24) Schmidt, P. W. In *The Fractal Approach to Heterogeneous Chemistry*; Avnir, D., Ed.; John Wiley & Sons: New York, 1989; p 67.
(25) Guo, X. H.; Zhao, N. M.; Chen, S. H.; Teixeira, J. *Biopolymers* **1990**, *29*, 335.
(26) Sinha, S. K.; Freltoft, T.; Kjems, J. In *International Topical Conference on Kinetics of Aggregation and Gelation*; Elsevier Science Publishers B.V.: Athens, GA, 1984; p 87.
(27) Bushell, G.; Amal, R. *J. Colloid Interface Sci.* **1998**, *205*, 459.
(28) Jullien, R. *J. Phys. I* **1992**, *2*, 759.
(29) Khlebtsov, N. G.; Melnikov, A. G. *J. Colloid Interface Sci.* **1994**, *163*, 145.
(30) Lin, M. Y.; Klein, R.; Lindsay, H. M.; Weitz, D. A.; Ball, R. C.; Meakin, P. *J. Colloid Interface Sci.* **1990**, *137*, 263.

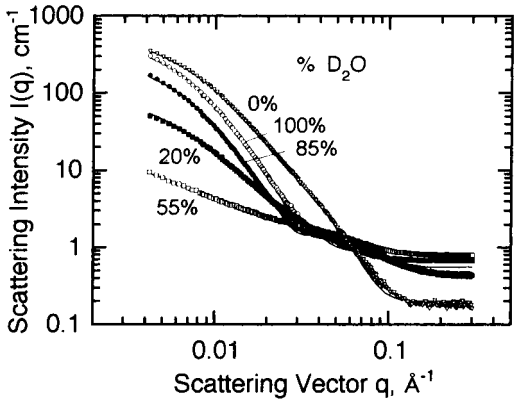

Figure 2. Five-parameter global fit of SANS data for magnetic fluids stabilized using protonated primary and secondary surfactants and dispersed in water with different H_2O/D_2O ratios. The symbols represent the experimental data, and the solid lines show the best model fit.

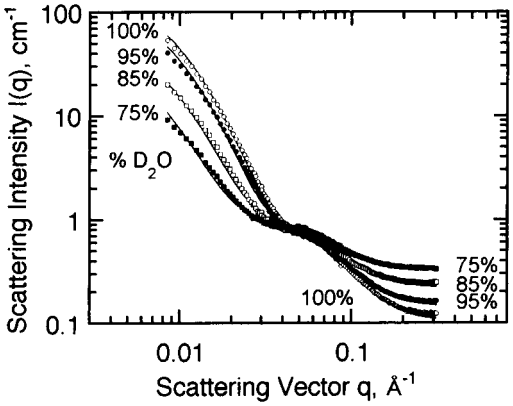

Figure 3. Two-parameter global fit of SANS data for magnetic fluids stabilized using deuterated primary surfactants and protonated secondary surfactants in water with different H_2O/D_2O ratios. The symbols represent experimental data, and the solid lines show the best model fit.

the intensity no longer reflects the aggregate size.[31] Indeed, when $q\xi \gg 1$ a power-law relationship for the angular variation of scattering, $I(\theta) \propto q^{-D}$ (over the range of $R \ll q^{-1} \ll \xi$), indicates internal variations in structure over lengths comparable to q^{-1}. Therefore, light scattering beyond the range of Guinier's law yields information about the microstructure within the aggregates. This provides the basis for experimental determination of the fractal dimension of large aggregates by static light scattering.[32]

4. Results and Discussion

SANS spectra were collected for a range of magnetic fluids having different combinations of deuterated and protonated primary and secondary surfactant layers and different solvent contrasts as determined by the ratio of protonated to deuterated solvent used in the magnetic fluid preparations. Both aqueous and organic-based magnetic fluids were studied. The large number of parameters in the models used to fit the SANS spectra (characterizing the particle size and polydispersity, the surfactant layer thicknesses, and the fractal properties of the clusters) usually prohibits the extraction of reliable parameter values by curve fitting. In our experimental design, however, up to five different SANS spectra with widely varying contrasts to emphasize different features of the magnetic fluids were fit simultaneously to obtain reliable estimates of all parameters describing the features of interest in our fluids. In the sections that follow, we discuss the extraction of the model parameters from the SANS spectra in more detail. Significant differences between the aggregate structures in surfactant bilayer-stabilized aqueous and monolayer-stabilized organic magnetic fluids are observed and are interpreted in terms of the relative strengths of the isotropic van der Waals, electrostatic, and steric interactions and the direction-sensitive magnetic dipole−dipole interactions in assembled clusters for the different systems. These discussions are supported by light scattering measurements on diluted aqueous magnetic fluids.

4.1. SANS Spectra and Model Fitting. The SANS spectra for aqueous and organic magnetic fluids having different levels of solvent deuteration at a concentration of 2.5 wt % are shown in Figures 2−4. It is clear that the curves differ markedly depending on the contrast ratio

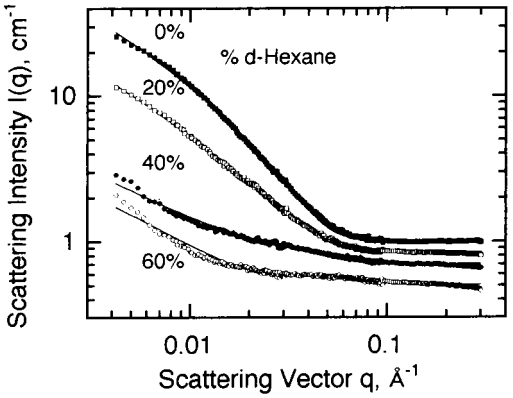

Figure 4. SANS spectra of organic-solvent-based magnetic fluids with varying levels of solvent contrast.

and, for the aqueous systems, on whether the two surfactant layers are both protonated or one is protonated and the other deuterated. The differences in these spectra are sufficient to provide discrimination between the two shell structures and the particle cores. A Guinier plot of the data ($\log[I(q)]$ versus q^2, not shown) indicated clearly that there is no simple characteristic length scale for the magnetic fluid suspensions,[33,34] an observation often attributed to polydispersity and/or interparticle interactions. Indeed, as the spectra in Figures 2−4 show, form factor oscillations are damped out because of smearing, largely caused by the polydispersity of the magnetic particles, which are known from earlier TEM measurements to have a log-normal size distribution. The inclusion of such polydispersity effects in accordance with eq 6 provides good matching of the simulated and experimental spectra in the high-q region. Simulations of the low-q region in which no interparticle interactions were allowed or in which hard sphere interactions only were included[23] were unable to account for the shapes of the spectra in the low-q region, even for concentrations as low as 0.2 vol %. In contrast, we found that the fractal clustering model accounted well for the observed behavior in the low-q regime, easily capturing the strong intensity variations with q.

On the basis of these considerations, the model described in section 3 was used for the nonlinear least-squares fits,

(31) Vacher, R.; Woignier, T.; Pelous, J.; Courtens, E. *Phys. Rev. B* **1988**, *37*, 6500.
(32) Russel, W. B.; Torres, F. E.; Schowalter, W. R. *J. Colloid Interface Sci.* **1991**, *142*, 554.
(33) Guinier, A.; Fournet, G.; Walker, C. L., Jr.; Yudowitch, K. L. *Small-Angle Scattering of X-rays*; Wiley: New York, 1955.
(34) Glatter, O.; Kratky, O. *Small-Angle X-ray Scattering*; Academic Press: New York, 1982.

in which the χ^2 error between the model and scattering data was minimized. Interparticle interactions were modeled using the fractal structure formulation described above, but for the intraparticle form factor two additive components, due to magnetic and nuclear scattering, were incorporated in our model, smeared using a log-normal distribution to account for the polydispersity. Different nuclear and magnetic scattering core radii were used in the analyses to account for the presence of an approximately 8.3-Å-thick nonmagnetic layer on the iron oxide surface.

4.1.1. Aqueous Magnetic Fluids. Modeling of the nuclear scattering was based on the proposed core−shell structure, in which we assumed uniform shells with SLD values that depended on the sample deuteration. The physical dimensions of the shells were assumed to be unaffected by the H_2O/D_2O solvent ratios. Because the contrast between fully protonated surfactants and the solvent is small relative to their individual contrasts with the particle core, the majority of the scattering in H_2O systems was from the iron oxide core itself. With D_2O as the solvent, it was the protonated surfactant shell that provided the strong contrast, yielding a scattering profile emphasizing the shell structure. At intermediate H_2O/D_2O solvent ratios, the relative importance of the core and surfactant shell changed, allowing for different scattering profiles yet again. Discrimination between the two concentric surfactant shells with different inner and outer radii was made possible by deuteration of only one of the two surfactant layers. At least five parameters (the iron oxide core radius R_C, its standard deviation σ, the surfactant bilayer thickness t, and the fractal dimension D and correlation length ξ of the fractal aggregates) were required to describe each of these systems. We therefore employed the contrast variation technique to generate multiple sets of independent experimental data, each emphasizing different features of the magnetic fluid suspension, as described above, and performed global fits to the data simultaneously using the core−shell model. With the five curves in Figure 2, all characterized by different solvent SLDs and a protonated surfactant bilayer, we obtained the iron oxide core radius R_C (41.3 ± 0.9 Å) and its standard deviation σ (14.9 ± 0.5 Å), the thickness of the surfactant bilayer t (24.8 ± 2.0 Å), and the fractal dimension D (2.52 ± 0.09) and correlation length ξ (341 ± 32 Å) of the fractal aggregates.

Clearly, the bilayer thickness estimated here is substantially less, by about 7 Å, than the total length for an all-trans extended conformation of primary and secondary surfactants, ∼32 Å. This difference is a result of strong curvature effects and is consistent with calculations based on TGA-measured surfactant coverages if we assume compact packing of the surfactants within the bilayer with no solvent (water) penetration.[6] The fitting results also suggest that the clusters, having a fractal dimension of 2.5, are fairly loose, three-dimensional, stable structures. Aggregation numbers for the particles in a cluster can be calculated from the relation $N_{agg} = (\xi/R)^D$,[25] from which we estimate that each cluster contains about 50 particles. These estimates are consistent with the cryo-TEM results shown in Figure 5, in which clusters having a typical size of 300 Å and containing about 20−50 particles are clearly evident, although they are not monodisperse. We show later that the cluster sizes estimated here are confirmed also by dynamic light scattering measurements.

The thickness of each of the surfactant layers in the bilayer was estimated by using a two-parameter global fit using four independent spectra for magnetic fluids having deuterated primary and protonated secondary surfactant layers with different D_2O/H_2O solvent ratios (Figure 3). In these fits, we held R_C, σ, D, and ξ at the values obtained in the first set of fittings described above. We obtained values of $t = 26.1 \pm 0.6$ Å for the bilayer thickness and $t_1 = 12.7 \pm 0.9$ Å for the thickness of the primary layer. These are the values expected for compact surfactant layers, and they support the validity of using a two-shell model to describe the microstructure of the self-assembled surfactant bilayer. The good agreement between the thicknesses of the bilayers obtained by two independent fitting processes confirms the internal consistency of our model. We cannot tell from these results to what degree the hydrocarbon chains of the two surfactants interpenetrate, although it is reasonable to assume that some interpenetration will occur, as inferred from our earlier DSC results and from the measured degree of solvent penetration of the single surfactant layers in organic magnetic fluids discussed below.

The relative importance of the intra- and interparticle contributions to the neutron scattering profiles can be seen in Figure 6, which shows plots of $F(q)$ and $S(q)$ versus q. In the small-q range, the interparticle structure factor, $S(q)$, accounted well for the large variations in the observed scattering intensity with changing q. Over the same q range, $F(q)$ showed little variation with q as individual particle feature sizes here were smaller than q^{-1}. For $q > 0.02$ Å^{-1}, the interparticle structure factor is close to

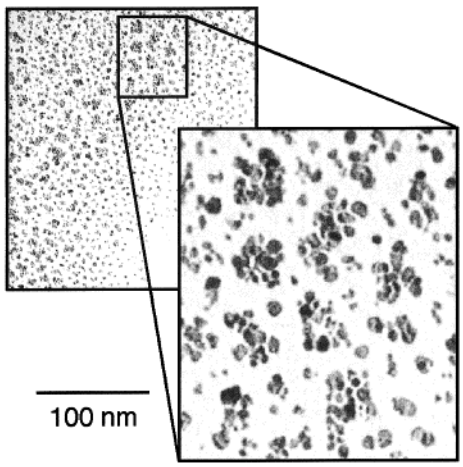

Figure 5. Cryo-TEM photograph of clusters in an aqueous magnetic fluid suspension.

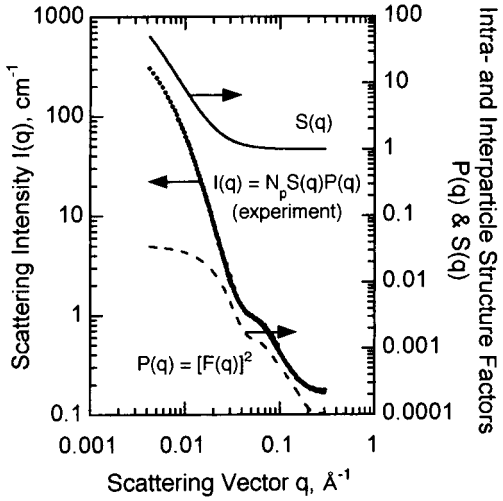

Figure 6. Predicted form factor $P(q) = [F(q)]^2$ and structure factor $S(q)$ for 100% D_2O-based magnetic fluids. The SANS spectrum for the sample is shown for comparison.

unity and the characteristic peaks for the microstructure of the magnetic nanoparticles are evident in the $F(q)$ function. The fitting model was sensitive to ξ, D, and $R = R_C + t$ in the low-q range and to R_C, σ, and t at the higher q values and was robust in its ability to capture unambiguously the various features of the magnetic fluids.

4.1.2. Organic-Solvent-Based Magnetic Fluids. For the organic-solvent-based magnetic fluids, we accounted for penetration of the lyophilic surfactant shell by the solvent alkyl chains by treating the volume fraction of solvent in the surfactant shell as a fitting parameter. (This possibility was discounted in the aqueous magnetic fluids because of the hydrophobic aversion of the surfactant shell for water penetration.) The primary surfactant layer coverage on the iron oxide surface determined by thermal gravimetric analyses and confirmed above in the SANS analysis of water-based systems was used to relate the surfactant shell volume and the volume fraction of the solvent in the shell through mass balances and geometric considerations of the structure.

Five unknowns were extracted during the multiparameter regression on the data from the contrast variation experiment (Figure 3). The average particle size (R_C = 40.7 ± 0.96 Å) and size distribution (σ = 10.6 ± 0.1 Å) are in good agreement with those obtained in the aqueous dispersions. Approximately 20.1% of the volume in the surfactant shell was occupied by penetrating solvent molecules, from which, using simple geometric arguments, we estimate that the penetration depth was about 5−6 Å. This depth is similar to the interpenetration zone inferred for the two surfactant layers in the bilayer structure of aqueous magnetic fluid particles using DSC.

The internal structure of these aggregates was characterized by a fractal dimension of 1.22 ± 0.08 and a correlation length of 424 ± 36 Å, which correspond to clusters having aggregation numbers of 8−12 particles. A fractal dimension of close to unity indicates the formation of magnetic particle chains, in contrast to the more compact clusters observed for aqueous magnetic fluids, which have a fractal dimension of 2.5. The possible reasons for this difference, such as changes in the relative importance of the various isotropic and directional interparticle forces acting on any two approaching particles and the effects of small aggregation numbers on the statistical evolution of the fractal dimension, are discussed below.

4.2. Cluster Formation and Growth.

4.2.1. Particle−Particle Interactions. The primary forces responsible for the particle−particle interactions are long-range van der Waals and electrostatic interactions, steric effects owing to the overlapping of the surfactant layers of two approaching particles,[35,36] and magnetic dipole−dipole interactions.[1−3] Of these interactions, the first three are isotropic whereas the dipole−dipole interactions are directional, that is, anisotropic. The interaction energies can be estimated as a function of the separation distance between two particles using suitable models for these interactions.

The van der Waals interaction energy, u_{vdw}, for two particles consisting of spherical core−shell structures interacting across a solvent medium is given by[37]

$$-12u_{vdw} = (A_m^{1/2} - A_s^{1/2})^2 H\left(\frac{s-2\delta}{d+2\delta};1\right) + (A_s^{1/2} - A_p^{1/2})^2 H\left(\frac{s}{d};1\right) + 2(A_m^{1/2} - A_s^{1/2})(A_s^{1/2} - A_p^{1/2}) H\left(\frac{s-\delta}{d};\frac{d+\delta}{d}\right) \quad (11)$$

where

$$H(x;y) = \frac{y}{x^2+2xy+x} + \frac{y}{x^2+2xy+x+y} + 2\ln\frac{x^2+2xy+x}{x^2+2xy+x+y} \quad (12)$$

The quantities A_p, A_s, and A_m represent Hamaker constants for the particles, surfactants, and medium, respectively. Note that for the organic systems, because the surfactant shell and the solvent medium have essentially the same Hamaker constants, only the van der Waals interactions between the iron oxide cores themselves are important, and the surfactant shells do not contribute to these interactions. The particle core surface-to-surface spacing is given by s, and the surfactant (bi)layer thickness is given by δ; the iron oxide core particle diameter is given by d.

The electrostatic interactions between two particles are present only in aqueous magnetic fluids and are due to the charge interactions between dissociated carboxylic acids on the surfaces of the two approaching particles. The charge densities on the particle surfaces are self-regulated,[38] however, and change as a function of the interparticle distance. A reasonable approximation for the interaction energy, u_e, as a function of interparticle distance was derived by Reiner and Radke[39] using the linear superposition approach:

$$u_e = 2\pi\epsilon\epsilon_0(\psi^\infty)^2\frac{2}{2+(h/a)}\exp(-\kappa h) \quad (13)$$

where $h = s - 2\delta$, $\psi^\infty = eC_t^s\eta a/\epsilon\epsilon_0[(1+\varsigma)\kappa a + 1]$ is the surface potential of an isolated particle, and $\varsigma = (eC_t^s/\epsilon\epsilon_0\kappa)(e\chi/kT)$, $\eta = -K_1'/(1+K_1')$, and $\chi = K_1'/(1+K_i')^2$ are derived from the linearized equilibrium relation for the carboxylic acid dissociation reaction. Here, C_t^s is the surface density of carboxyl groups at the surfactant−water interface, κ is the inverse Debye length, e is the electronic charge, and ϵ and ϵ_o are the dielectric constant and permittivity of free space, respectively. Also, k is the Boltzmann constant, and T is the temperature. The effective dissociation ratio $K_1' = [COO^-]/[COOH]$ satisfies the expression $\log_{10} K_1' = pH - pK_a$.

We do not provide estimates of the steric interactions near the point of closest approach, as the complex interactions in this region cannot be modeled satisfactorily. Indeed, it is generally accepted that although the barrier height and position are described reasonably well by the combined van der Waals and electrostatic models according to the Derjaguin−Landau−Verwey−Overbeek analysis, these models also break down close to particle−particle contact, and the attractive well cannot be modeled with confidence.

The magnetic dipole−dipole interaction energy, u_{ij}, is given by[1,40]

(35) Israelachvili, J. *Intermolecular & Surface Forces*: *With Applications to Colloidal and Biological Systems*, 1st ed.; Academic Press: San Diego, CA, 1985.
(36) Hiemenz, P. C. *Principles of Colloid and Surface Chemistry*, 2nd ed.; Marcel Dekker: New York, 1986.
(37) Vold, M. J. *J. Colloid Sci.* **1961**, *16*, 1.
(38) Carnie, S. L.; Chan, D. Y. C. *J. Colloid Interface Sci.* **1993**, *155*, 297.
(39) Reiner, E. S.; Radke, C. J. *Adv. Colloid Interface Sci.* **1993**, *47*, 59.

$$u_{ij} = \frac{m^2}{4\pi\mu_0 r_{ij}^3}[\mathbf{n}_i\cdot\mathbf{n}_j - 3(\mathbf{n}_i\cdot\mathbf{r}_{ij})(\mathbf{n}_j\cdot\mathbf{r}_{ij})] \qquad (14)$$

where $\mathbf{r}_{ij}$ is the particle center-to-center unit vector, $\mathbf{n}_i$ is the unit vector of the magnetic dipole of particle i, m is the particle dipole moment, and μ_0 is the magnetic permittivity of free space. The orientations are randomized to some extent because of thermal kinetic energy effects, with the orientational distribution skewed toward the more energetically favorable energy state of end-to-end alignment of the magnetic dipoles. The effective magnetic interaction energy is then given by the Boltzmann averaged magnetic dipole−dipole energy, u_{mag}, which takes into account these preferred dipole orientation distributions:[40]

$$u_{mag} = -2/3\frac{m^4}{(4\pi\mu_0)^2 r^6 kT} \qquad (15)$$

Figure 7a shows the interaction profiles for organic-based magnetic fluids stabilized by single surfactant layers and Figure 7b shows the corresponding results for aqueous systems in which a stabilizing surfactant bilayer is present, for representative values of the system parameters. In both cases, the interaction energies are shown as a function of the distance between the iron oxide particle cores. The shaded region lies between the limiting cases in which the surfactants are either fully compacted within the surfactant (bi)layer or fully extended. This zone is the interpenetration region for opposing surfactant layers as the particles approach each other and gives rise to steric interactions which contribute a repulsive component to the total energy profile and which cannot be reliably estimated, as discussed above.

The magnetic dipole−dipole interaction profiles are the same for both aqueous and organic-based magnetic fluids, but the van der Waals interaction profiles differ considerably. For the organic-based systems, the surfactant tail groups are essentially indistinguishable from the solvent and therefore do not contribute to the overall van der Waals interactions. The oriented dipole−dipole interactions contribute about 15% to the total interaction energy and tend to favor chain formation, although only very weakly. The magnitude of the total interaction energy on particle−particle contact is of the order of $1-2\ kT$, which indicates that the aggregates are susceptible to breakup by thermal forces. The sizes (correlation lengths) of the aggregates, or the aggregation numbers, will be fairly small, therefore, as is observed experimentally. Monte Carlo simulations are in good agreement with these observations.[41]

For the aqueous magnetic fluids, the surfactants *do* contribute to the overall attractive van der Waals interactions because their dispersion properties are different from those of the surrounding solvent, water. Electrostatic interactions also play a role, of course, and it is clear from the profiles shown in Figure 7b that the isotropic van der Waals and electrostatic interactions are dominant, whereas the directional dipole−dipole interactions play little or no role in the aggregation process. These isotropic interactions do not favor growth in any one direction, and because the energy barrier to clustering is sufficient to ensure the clustering is reaction-limited but not sufficient to prohibit

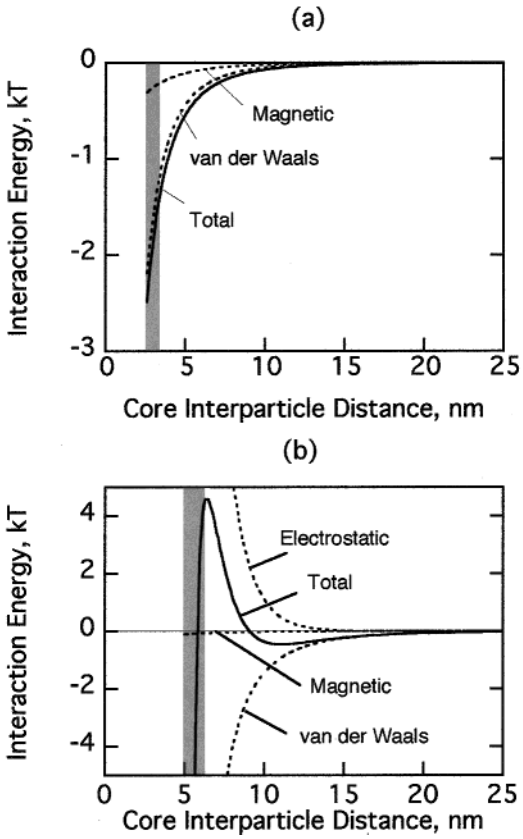

Figure 7. Theoretical estimates of particle−particle interaction energies for (a) organic and (b) aqueous magnetic fluid systems. $d = 10^{-8}$ m, $A_p = 5.09 \times 10^{-19}$ J, $A_m = 4.15 \times 10^{-19}$ J, $A_s = 2.17 \times 10^{-20}$ J, $n = 0.05$ M ($\kappa = 7.36 \times 10^{-8}$ m^{-1}), $K_1' = 2.72$, $C_t^s = 2.27 \times 10^{18}$ m^{-2}.

such clustering (i.e., $<15\ kT$ [42]), we expect the clusters to be loose, three-dimensional structures as observed in our SANS studies. It is possible that the magnetic interactions between aggregated particles lead to some directional orientation of the particles within the cluster, so that the cluster itself may have a significant dipole moment. These particles are not strongly coupled magnetically, however, as demonstrated by our SQUID results reported earlier and as would be anticipated based on the weakness of the interactions shown in Figure 7. There is a delicate balance between the electrostatic and van der Waals interactions, and it is well-known that small changes in the solvent ionic strength, for instance, can have significant effects on the stability of the dispersion.

4.2.2. Particle−Cluster Interactions and Finite Cluster Sizes. The aqueous clusters reach a finite size of approximately 50 particles per cluster and do not grow further once this size is attained, probably because the cluster growth rate decreases dramatically as the clusters become larger. The precise structure and charge distribution within the cluster are not known, although it is reasonable to assume that the particles in the body of the cluster have relatively low charge owing to charge regulation and that those on the surfaces are highly charged. A primary particle approaching the cluster will interact with a number of particles near the surface of the cluster. Curvature effects will ensure that these interactions increase with increasing cluster size, just as the interaction of a particle with a planar surface is much more pronounced than that with another primary particle

(40) Tester, J. W.; Modell, M. *Thermodynamics and Its Applications*; Prentice Hall: Upper Saddle River, NJ, 1997.
(41) Fateen, S. K.; Rutledge, G. C.; Hatton, T. A. In preparation.
(42) Vold, R. D.; Vold, M. J. *Colloid and Interface Chemistry*; Addison-Wesley: London, 1983.

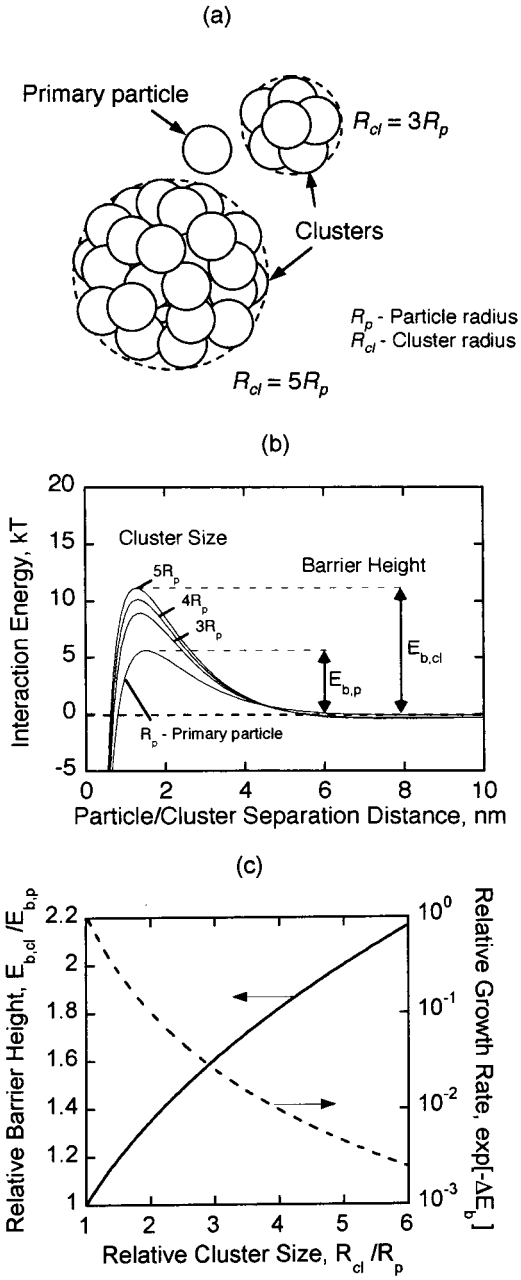

Figure 8. Particle−cluster interactions in aqueous magnetic fluids: (a) relative sizes of particles and clusters, (b) theoretical estimates of particle−cluster interaction energies as a function of separation distance, and (c) relative barrier height for particle−cluster interactions as a function of cluster size. $R_p = 5 \times 10^{-9}$ m, $\kappa = 7.36 \times 10^{-8}$ m^{-1} ($n = 0.05$ M), $C_t^s = 2.27 \times 10^{18}$ m^{-2}, $A_p = 1 \times 10^{-19}$ J.

as discussed below. It is suggested here that this increasing barrier with increasing cluster size is the reason for the size limitation on cluster growth.

As a first approximation, we can treat the cluster as a large particle of radius R_{cl} ($\sim\xi$) and given surface potential interacting with a primary particle of radius R_p as it approaches the cluster, as indicated schematically in Figure 8a. The distance between the particle and the cluster indicated in this figure corresponds to the separation at which the particle/cluster interaction energies are the largest, as estimated below; particles closer than this distance will be trapped and assimilated by the cluster, causing further cluster growth. The change in the barrier height, E_b, and hence also in the rate of attachment of individual particles to the clusters [$\sim\exp(-E_b)$] can be estimated by considering a simple model of the electrostatic and van der Waals interactions between two spheres of different sizes. If we assume that the surface potentials, ψ^∞, of all particles and clusters are constant and equal, then the variation of the electrostatic interaction energy with interparticle distance, s, can be approximated by a simplified form of the equations given by Hogg et al.,[43] that is, by

$$u_e = 4\pi\epsilon\epsilon_0\left(\frac{R_p R_{cl}}{R_p + R_{cl}}\right)(\psi^\infty)^2 \ln(1 + \exp(-\kappa s)) \quad (16)$$

This simple result indicates that as R_{cl}/R_p increases, the electrostatic interaction energy increases; the electrostatic interaction energy for the particle with a plane, for instance, is double that for interactions between two particles having the same surface properties.

Similarly, we can approximate the van der Waals interactions by treating the particles and clusters as uniform spheres of constant effective Hamaker constant, A_{eff}, according to

$$-12u_{vdw} = A_{eff}H\left(\frac{s}{2R_p};\frac{R_{cl}}{R_p}\right) \quad (17)$$

The effective Hamaker constant for the interaction of the particle with the cluster depends on the particle density within the cluster and in particular on the particle density near the cluster surface, as the void spaces are filled with solvent and do not contribute to the particle/cluster interactions. We assume that we can approximate these interactions through some Hamaker constant averaged over the particle cluster through the expression

$$A_{eff} = (A_p A_{cl})^{1/2} = \sqrt{f}A_p \quad (18)$$

where f, the volume fraction of particles in the cluster, can be estimated in terms of the fractal dimension through the equation $f = (R_p/R_{cl})^{3-D}$.

Figure 8b shows the interaction energy profiles for different cluster sizes. The parameter A_p was selected to ensure that the profile for the particle/particle interactions matched that calculated using the more detailed models discussed above. It is clear that the effective barrier height for particle/cluster interactions, shown in Figure 8c, increases as the cluster size increases, that the relative cluster growth rate decreases sharply with increasing cluster size, and hence that there should be a finite cluster size at which further growth of the clusters is severely restricted. The value of $E_b = 11.5\ kT$ for a cluster of size $R_{cl} = 5R_p$ (corresponding to the cluster sizes observed experimentally) is lower than the accepted value of approximately 15 kT at which the energy barrier is insurmountable.[42] It should be noted, however, that the simplifications in the model treatment do not permit quantitative estimates to be made of the change in barrier height, although the relative magnitudes of the effects are relevant to this discussion. In particular, the assumption of equal and constant surface potentials for the clusters and particles is questionable, and a more detailed analysis of the van der Waals interactions should take into account the precise distribution of the primary particles in the cluster. Nevertheless, it is evident from this analysis that the changing interaction potentials between a particle and a cluster as the cluster grows can

(43) Hogg, R.; Healy, T. W.; Fuerstenau, D. W. *Trans. Faraday Soc.* **1966**, *62*, 1638.

play an important role in limiting the growth rate and hence the size of the clusters formed and thereby in providing kinetic stability to the suspension.

4.2.3. Fractal Aggregates. In many cases, the structures of fractal aggregates can be interpreted in terms of the relative balance between diffusional and reactive (or adhesive) limitations. For diffusion-limited systems, a particle sticks to the first particle it encounters in a cluster and the cluster growth normally results in loose, extended aggregates of fractal dimension ~1.8.[44] In contrast, reaction-limited systems tend to yield more compact structures as the particle can sample a significant portion of the open regions surrounding the cluster before adhering to it. Reaction-limited systems are generally characterized by a fractal dimension on the order of 2.1; the higher values observed here indicate a slower restructuring process once the clusters are formed. The aqueous magnetic fluid behavior is consistent with this latter argument, as the electrostatic barrier to clustering limits the cluster growth rate, and we observe fractal dimensions consistent with loose, three-dimensional growth. On the other hand, for the organic systems the adhesion forces are small, comparable to thermal forces, so that although there is no barrier to aggregation, the collide-and-stick model is not a valid description either. In this case, the directional magnetic forces may be weakly responsible for the observed cluster structure, as intimated above, leading to lower fractal dimensions, but this is unlikely to be the sole cause of apparent chain formation. Indeed, literal interpretation of the fractal model for such low aggregation numbers must be viewed with caution as application of the equation relating the fractal dimension, aggregation number, and aggregate size, that is, $D = (\ln N_{agg})/\ln(\xi/R_p)$, to reasonably compact small aggregates of aggregation numbers less than about 10−20 can still yield low numbers for the fractal dimension even in the absence of preferred directional interactions. For instance, tightly packed structures having two, three, and four particles have fractal dimensions of 1, 1.59, and 2, respectively, and these fractal dimensions fall quickly when the packing constraints are relaxed, which would certainly be the case when the attractive interparticle interactions are small as in this example. In such cases, the small forces ensure not only small aggregation numbers but also a random movement of particles about the cluster, leading to looser aggregates than would be obtained in the presence of strong particle−particle interactions, and hence lower apparent fractal dimensions. A cluster of eight particles, for instance, with a maximum correlation length of four particle radii will give a fractal dimension of 1.5, whereas if the correlation length corresponds to five particle radii, a fractal dimension of 1.29 is obtained. Monte Carlo simulations indicate that such structures are readily obtained even in the absence of directional forces between the particles. Thus, it is likely that the low fractal dimensions obtained for organic systems are a direct consequence of the small aggregates formed because of weak interparticle interactions and the constraints on the packing of particles in these small clusters.

4.3. Comparison of Particle Sizes Measured Using Different Techniques. There are discrepancies between the iron oxide core radii and standard deviations obtained using different techniques, namely, TEM, magnetization measurements, and SANS (Table 2), that must be reconciled. We have already noted that the difference between the physical sizes and the magnetic core radii of magnetic nanoparticles is due to the presence of a disordered nonmagnetic metal oxide layer on the particle surface and the difference between the TEM and magnetization measurements is consistent with these observations.

Table 2. Particle Size and Size Distribution of the Iron Oxide Core Obtained by TEM, Magnetization, and SANS Measurements

	TEM	magnetization	SANS
mean radius R (Å)	46.5	36.0	41.3
standard deviation σ (Å)	13.0	11.0	14.9

The approximately 12% difference in actual core radii determined using TEM and SANS can be attributed to the shapes of the iron oxide cores. Many of the magnetic particles seen on TEM micrographs are clearly nonspherical and can be better described as ellipsoids than as the spheres assumed in our SANS model. The reported TEM radii were obtained as the arithmetic average of the longer and shorter dimensions of the particles, that is, were calculated using $R = (1 + a)r/2$ assuming uniform ellipsoids having principal Cartesian semi-axes (r, r, ra).[45] It can be shown that the scattering of neutrons by prolate ellipsoids is equivalent to the scattering from a system of polydisperse spheres having a mean radius R smaller than $(1 + a)r/2$. For a prolate ellipsoid with $a = 1.5$, for instance, the equivalent sphere size measured using SANS would be about 15% smaller than the size we would report for TEM measurements on the same particles. In this study, then, the shape effect could be significant and explains the discrepancy between our SANS and TEM radii.

4.4. Fractal Aggregates in Diluted Magnetic Fluids. Light scattering can be used to probe the internal structure of large aggregates and provide complementary information to supplement our SANS results, provided of course that the solutions do not attenuate the light beam significantly. The magnetic fluids are dark and opaque at the typical concentrations used in our SANS studies, however, and at least a 100-fold dilution of the magnetic fluids with water was required to make them suitably transparent to permit light scattering experiments to be performed reliably. When the magnetic fluids were diluted with pure water, the particle clusters increased dramatically in size and continued to grow with time, indicating a destabilization of the magnetic fluid suspension upon dilution. The hydrodynamic radii determined 1 h after dilution are shown in Figure 9 and are seen to increase with increasing addition of water. A likely reason is that the stabilizing charged secondary surfactant layer was partially stripped from the particle surfaces on dilution. We estimated from experimental partitioning data that approximately 6% of the secondary surfactant remained on the particle surface when the particles were diluted to a volume fraction of 4×10^{-6} and 3% remained upon a further 2-fold dilution. The incompatibility between the exposed primary surfactant hydrocarbon tails and surrounding water caused the magnetic particles to aggregate and, with time, to form clusters sufficiently large to precipitate from solution.

The apparent cluster sizes ξ determined for magnetic fluids diluted with pure water to volume concentrations of 2×10^{-6} and 4×10^{-6}, respectively, are sufficiently large after 1 h to satisfy the criterion $R \ll q^{-1} \ll \xi$ in static light scattering measurements. Under these conditions, when the intensity is plotted as a function of q on a log−log plot as in Figure 10, the slope of the curve represents

(44) Russel, W. B.; Saville, D. A.; Schowalter, W. R. *Colloidal Dispersions*; Cambridge University Press: New York, 1989.

(45) *Physics of Amphiphiles: Micelles, Vesicles, and Microemulsions*; Degiorgio, V., Corti, M., Eds.; North-Holland: New York, 1983.

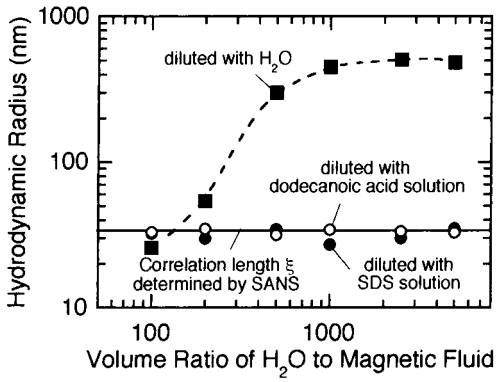

Figure 9. Hydrodynamic diameters of magnetic nanoparticles diluted with pure water and with aqueous surfactant solutions (SDS and dodecanoic acid) determined by dynamic light scattering.

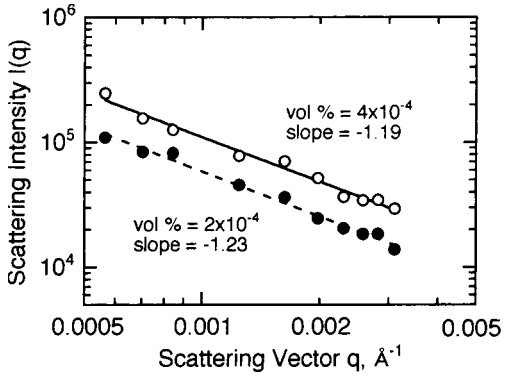

Figure 10. Static light scattering intensity distributions for magnetic fluids diluted with pure water. In this power-law regime, the negative of the slope represents the fractal dimension for the aggregates.

the fractal dimension of the aggregates. A fractal dimension of 1.20 ± 0.11 was obtained for the two different concentrations, indicating that the internal structure of these flocs is more similar to that in the organic solvent than to that in the concentrated aqueous particle suspensions. It is likely that the clusters themselves participate in this growth process and not the individual particles, which can be reasonably assumed to remain in their original clustered state. Thus, we surmise that the aggregates are chains of primary clusters, each containing about 50 particles. With the almost complete desorption of secondary surfactant from the particle surface, the electrostatic barrier to aggregation is removed, and the clusters adhere on contact owing to the strong van der Waals interactions. For the chainlike structures observed here, the fractal dimension is somewhat lower than the customarily reported theoretical lower limits of 1.7−1.8. In analogy with the results for clustering in organic solvents, we conclude that this level of clustering could be a result of a weak, nonisotropic interaction, akin to the magnetic dipole−dipole interactions discussed above, as well as of the small number of clusters participating in the aggregate. A partial mutual alignment of the particle magnetic moments in the clusters could lead to a measurable overall moment for each cluster and hence to a directional component to the interactions between the clusters and the growing aggregates. On the other hand, the total number of clusters participating in this larger aggregate (15−20) is fairly small, such that, statistically, smaller apparent fractal dimensions are observed than would be the case for much larger aggregates.

Desorption of the secondary layer from the particle surfaces was repressed by diluting the magnetic fluid with a surfactant solution at concentrations close to or above its critical micelle concentration. Under these conditions, with both SDS and decanoic acid surfactant solutions, diluted magnetic fluid suspensions remained stable indefinitely. Moreover, the hydrodynamic radii of the clusters were unaffected by dilution with the surfactant solutions and remained constant at a value of about 350 Å (see Figure 9), close to the cluster correlation length of 340 Å determined by SANS for compact clusters. Further evidence for the stability of these clusters was provided by a series of experiments in which we observed that the clusters in these diluted solutions could be broken down by sonication but they grew again to their presonication sizes over periods of several minutes.

The organic magnetic fluids behaved differently from the aqueous systems when diluted with solvent. As the magnetic and van der Waals forces holding these clusters together are much weaker than the van der Waals interactions responsible for cluster stability in the aqueous systems, these clusters tended to dissociate when diluted to satisfy simple mass action laws, and no clusters were observed by light scattering.

5. Conclusions

We have probed the solution structure of surfactant-stabilized magnetite-based magnetic fluids in the absence of a magnetic field using small-angle neutron scattering and dynamic and static light scattering techniques. These results shed new light on the structures of both aqueous and organic magnetic fluids prepared with fatty acid stabilized magnetite nanoparticles and also confirm our earlier results on the particle and surfactant (bi)layer characteristics of dried particle preparations, inferred from thermal analyses.

In aqueous magnetic fluids, individual magnetic nanoparticles are stabilized by highly ordered self-assembled bilayers of the two alkanoic acids and cluster to form compact fractal structures with a fractal dimension D of 2.5. The cluster correlation length, ξ, of approximately 340 Å estimated using SANS is close to the hydrodynamic radius determined by dynamic light scattering and to the sizes of clusters observed directly in cryo-TEM experiments. Approximately 50 particles participate in these clusters. The bilayers themselves are compact structures consistent with interpenetration of the two surfactant layers to a depth of approximately 6 Å, as was inferred from earlier DSC experiments. Upon dilution with water, these clusters grew to form chainlike structures as the dispersion was destabilized because of the desorptive loss of secondary surfactant to the surrounding solvent (water) phase. When surfactant was added to the diluent phase to prevent this desorption, the particle cluster sizes were unchanged, indicating strong adhesive forces within these aggregates.

The behavior of the organic-solvent-based magnetic fluids was significantly different from that of the aqueous systems. The surfactant monolayer in this case was penetrated by the solvent to a depth of approximately 6 Å (20% volume fraction). Small chainlike clusters with fractal dimensions of about 1.2 formed, and the sizes of these clusters decreased upon dilution with the solvent phase in a manner consistent with mass action-controlled aggregation processes.

The strong contrast in the behavior of the two magnetic fluid systems can be attributed to the strength and nature of the dominant interaction energies in each cluster. In the organic-solvent-based magnetic fluids, the magnetic

dipole−dipole interactions contribute about 15% to the total interaction energy at the point of closest approach, which is determined by steric effects as the two surfactant layers begin to overlap. The most energetically favorable alignment of these particles is end-to-end, but this is not a dominant interaction because the energy is comparable to or smaller than the thermal energy, kT. It appears that the small fractal dimension is a consequence of the small cluster size, which in itself is a result of the weak van der Waals and magnetic interparticle forces. With aqueous magnetic fluids, however, the strong contribution of the surfactant bilayer to the van der Waals attractions and the electrostatic repulsions, which combined provide a finite energy barrier to clustering, dominate the interactions. The magnetic dipoles play essentially no role in determining the particle correlations within the isotropic cluster, and the larger clusters that are formed can take on more compact structures. The clusters themselves are limited in size because as they grow, their interactions with other particles and clusters become increasingly repulsive until the barrier height is sufficiently high that capture of a particle by a cluster is highly unlikely. For diluted aqueous systems, when the secondary surfactant layer can be stripped off the particle, the clustering process leads to the formation of unstable open structures characterized by low fractal dimensions.

Acknowledgment. We thank S. Kline (National Institute of Standards and Technology) for his assistance with the SANS measurements and are grateful to J. Hayter (Oak Ridge National Lab) and J. Barker (National Institute of Standards and Technology) for valuable discussions on the magnetic scattering of iron oxide. We also thank Paul Johnston and Arijit Bose (University of Rhode Island) for doing the cryo-TEM experiments. This material is based upon activities supported by the National Science Foundation under Agreement No. DMR-9423101. We acknowledge the support of the National Institute of Standards and Technology, U.S. Department of Commerce, in providing the neutron facilities used in this work.

LA9916732